DESIGN, IMPLEMENTATION AND FLIGHT TESTING OF A SUBSCALE DEMONSTRATOR FOR ASSESSING THE STALL BEHAVIOUR OF A LARGE SWEPT-WING RESEARCH UAV

B. Scheufele, S. J. Koeberle, M. Hornung
Institute of Aircraft Design, Technical University of Munich,
Boltzmannstraße 15, 85748 Garching, Germany

Abstract

The flying demonstrator *T-FLEX* for the assessment of active flutter suppression and load alleviation technologies is developed and flight tested during the projects *FLEXOP* and *FLiPASED*. In order to assess the stall behavior of the demonstrator without conducting the respective tests on itself, the scaled demonstrator *DeFStaR* was developed during a project work and Master's Thesis [1] in order to conduct respective flight tests. The scaling focused on aerodynamic scaling in terms of aerodynamic coefficients $C_{L\alpha}$ and $C_{m\alpha}$ as well as dynamic scaling in terms of center of gravity as well as mass moments of inertia. The scaling factor was finally determined to be 0.53. The design relied on commercial-off-the-shelf components whenever possible, while the wing was manufactured in-house in order to assure close geometric similitude. After implementation, ground and flight tests were conducted in order to assure dynamic and aerodynamic similitude, using bifilar pendulum tests for determining the mass moments of inertia as well as system identification techniques to verify the relevant aerodynamic derivatives of the demonstrator. Following stall tests showed a wide range of different behaviors from a "plunging" flight state, that allowed the pilot to maintain attitude, to a flat spin causing considerable loss of altitude.

Keywords

Remotely Piloted Aircraft System; RPAS; Unmanned Aerial System; UAS; Unmanned Aerial Vehicle; UAV; Dynamic Scaling; Subscale Demonstrator; FLEXOP; FLiPASED;*T-FLEX*; Horizon 2020; Stall Recovery; Flight Test

1. THE *T-FLEX* TECHNOLOGY DEMONSTRATOR

In 2016 development activities commenced in order to design, build and flight test a testbed for demonstrating emerging technologies such as active flutter suppression, aeroelastic tailoring, and gust as well as maneuver load alleviation in flight during the projects *FLEXOP* and *FLiPASED* as part of the European Union's *Horizon 2020* research and innovation programme [2, 3]. The resulting technology demonstrator *T-FLEX* is depicted in the following Fig. 1.

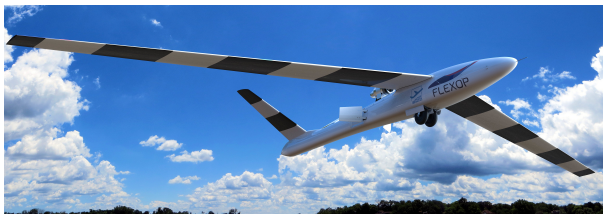

FIG. 1. Rendering of the demonstrator *T-FLEX*, developed during the project *FLEXOP* [4]

The design features peculiarities such as high aspect-ratio, swept wings, a slender fuselage with a tail-dragger landing gear setup, as well as a dorsal-mount turbine and airbrakes for realizing high longitudinal accelerations and an airspeed up to 65 m/s.
Due to the comparably high wing-sweep, it was suspected that a stall would commence at the wing tips which would lead to shift of neutral point (N.P.) in forward direction in front of the center of gravity (C.G.), creating an unstable configuration with disadvantageous stalling characteristics such as a sudden onset and pitch-up behavior. This mechanism is presented in Fig. 2.

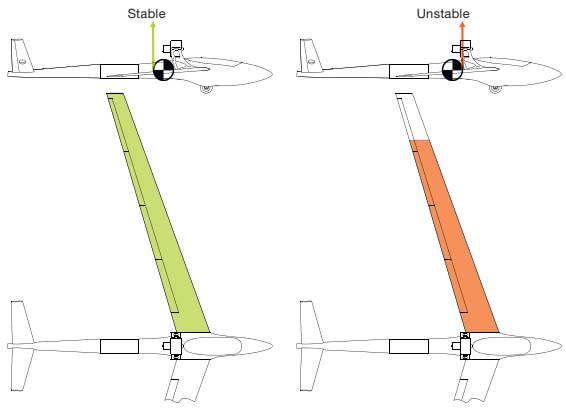

FIG. 2. Exemplification of the expected stall onset with resulting unstable configuration, attached flow is indicated with colors. Left: Nominal flight condition with fully attached flow, neutral point is located behind the C.G. Right: Wing stall commencing at the wing tips, causing the N.P. to move forward creating an unstable configuration. [1]

In order to avoid stall, a rather large safety margin is being maintained in terms of the operationally allowed airspeed,

doi: 10.25967/550035

which also results in higher take-off speeds that turned out to be problematic due to the ground handling qualities of the landing gear configuration. Therefore, in order to assess the stalling behavior of the configuration, a dynamic demonstrator was designed, built, flight tested and it's data assessed.
In the following sections, the methodology of dynamic scaling is introduced, the objective of the dynamically scaled model defined and the chosen design approach presented. The resulting design is described, together with planned tests. Finally, the results of the tests conducted are presented and discussed.

2. SUBSCALE DEMONSTRATORS IN RESEARCH AND DEVELOPMENT

In the context of aerospace, subscale flight testing (SFT) aims at using a smaller model, a subscale demonstrator of an aircraft, in order to gain knowledge about the full-scale aircraft. Typical goals are the evaluation of aerodynamic and mission performance, stability as well as controllability. A comprehensive review of existing projects has been presented by Sobron et al. [5], so that this section only showcases select projects. The approach of subscale demonstrators is typically applied in order to reduce the development and production cost of a full scale prototype [6]. Perhaps the most prominent use of dynamically scaled demonstrators is documented for the American *National Air and Space Agency* (NASA), which has used a variety of flying subscale models like the *T-2* demonstrator in the *Airborne Subscale Transport Aircraft Research* (*AirSTAR*) project among others. [7, 8]
In the environment of universities and industry, subscale demonstrators appeal with lower cost and fast development cycles: The Linköping University has conducted research using scaled flight testing with numerous projects such as the *ECO-Sport* [9] or *RAVEN* [10].
To be able to relate the results of the subscale demonstrator to the full-scale aircraft, the scaling has to conform to certain scaling laws. Aforementioned demonstrators have been designed using the principles of similitude, which also in the context of aircraft has been widely described with Grainer and Hoffmann [11] as well as Wolowicz et al. [12] being among the most prominent publications. As in order to achieve full physical similitude, a model has to achieve geometric, kinematic and dynamic similitude. This, however, is typically both practically impossible, because the necessary scaling laws contradict each other, and not necessary in order to realize similitude of the demonstrator in the relevant aspects [13]. Therefore, in the following, only the scaling as applied for the design of the *DeFStaR* demonstrator are being described in more detail.

3. DEMONSTRATOR DESIGN AND MANUFACTURE

The subject of the investigation is the assessment of the stall-behavior as well as the recovery process of the *T-FLEX* demonstrator. The stall-behavior primarily depends on the geometric airfoil shape, angle of attack α and Reynolds number. The recovery process depends on the rigid-body dynamics and aerodynamic forces. It was determined that the *DeFStaR* demonstrator needs to be scaled aerodynamically and dynamically. Wolowicz et al. [12] states different sets of of scaling laws for various applications. The set in Table 1 depicts an excerpt of the scaling laws for free flying models concerning the stall behavior and recovery where compressibility effects can be neglected due to low operational Mach number.

TAB. 1. Scaling laws concerning stall behavior and recovery [1].

No.	Parameter	Correlation
1	Length	$\frac{l_M}{l_A} = n$
2	Vehicle attitude	$\frac{\alpha_M}{\alpha_A} = 1$
3	Froude number	$\frac{\left(\frac{v^2}{lg}\right)_M}{\left(\frac{v^2}{lg}\right)_M} = 1$
4	Dynamic pressure	$\frac{q_M}{q_A} = \frac{\rho_M}{\rho_A}$
5	Reynolds number	$\frac{(Re_M)}{(Re_A)} = \left(\frac{v_A}{v_M}\right)^{\frac{3}{2}}$
6	Angular rate	$\frac{\Omega_M}{\Omega_A} = 1$
7	Time	$\frac{t_M}{t_A} = \sqrt{n}$
8	Angular displacement	$\frac{\varphi_M}{\varphi_A} = 1$
9	Angular acceleration	$\frac{\dot{\Omega}_M}{\dot{\Omega}_A} = \frac{1}{n}$
10	Linear displacement	$\frac{s_M}{s_A} = n$
11	Linear acceleration	$\frac{a_M}{a_A} = 1$
12	Strouhal number	$\frac{\left(\frac{\omega l}{v}\right)_M}{\left(\frac{\omega l}{v}\right)_A} = 1$
13	Oscillatory frequency	$\frac{\omega_M}{\omega_A} = \frac{1}{\sqrt{n}}$
14	Relative density factor	$\frac{\left(\frac{m}{\rho_c l^3}\right)_M}{\left(\frac{m}{\rho_c l^3}\right)_A} = 1$
15	Mass	$\frac{m_M}{m_A} = \left(\frac{\rho_{cM}}{\rho_{cA}}\right)^{n^3}$
16	Rel. mass moment of inertia	$\frac{\left(\frac{I}{\rho_c l^5}\right)_M}{\left(\frac{I}{\rho_c l^5}\right)_A} = 1$
17	Mass moment of inertia	$\frac{I_M}{I_A} = \left(\frac{\rho_{cM}}{\rho_{cA}}\right)^{n^5}$

Not all of these laws are reasonable as driving parameters for the design process as they are either set by test conditions, result from governing scaling laws or parameters measured during the flight test. From this set length, mass and mass moment of inertia are chosen as the governing scaling laws of the design process. Furthermore parameters like the stability coefficient $C_{m\alpha}$, lift coefficient $C_{L\alpha}$ as well as the the horizontal tail volume coefficient V_H were taken into account.

3.1. Design Methodology

The conceptional design phase was mainly effected by the legal constraint of a maximum take-off weight of 25 kg, in-house manufacturing capabilities and the availability of *commercial of the shelf* (COTS) components. In essence, this investigation indicated a scaling factor *n* between 0.3 and 0.53 driven by the weight of the necessary test instrumentation and equipment and the manufacturing capabilities

The objective of the preliminary design phase was to determine the most suitable scale factor considering the constraints determined in the conceptional design phase and achieving the best possible similarity regarding the stall behavior. Since chord length, stall speed and hence the Reynolds number changes, by scaling the aircraft, the progression of the lift coefficient $C_{l\alpha}$ and stability coefficient of the profile $C_{m\alpha}$ changes. In the detailed design phase a *Computer Aided Design* (CAD) model of the *DeFStaR* aircraft was planned, which is necessary for designing custom made components (wings, engine mount, equipment bay, etc.) and monitoring the C.G., mass and mass moment of inertia to assure feasibility of the demonstrator. Continuous comparison of the CAD-model with an simulation implemented in *XFLR5* [14] assured aerodynamic similitude on configuration level.

3.2. Analysis of Aerodynamic Coefficients of the Airfoil for the Determination of the Scale Factor *n*

The *T-FLEX* demonstrator is equipped with a trip band at the leading edge of the wing to force turbulent airflow. *DeFStaR* is designed to have the same feature which brings the advantage, that the assumption of turbulent airflow is justified even at the lower Reynolds numbers at which a subscale demonstrator is expected to Operate. Therefore, the simulation of the aerodynamic coefficients in *XFOIL* [15] needs to be solved for turbulent airflow. Figure 3 and 4 exhibit polars of the aerodynamic derivatives $C_{l\alpha}$ and $C_{m\alpha}$ of the 2D-airfoil shaping the wingtip of the *T-FLEX* demonstrator at various Reynolds numbers.

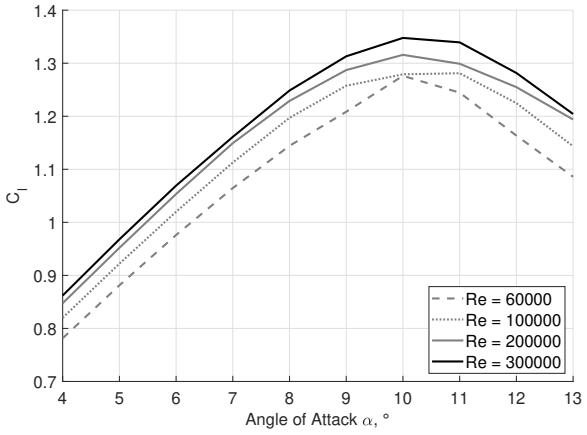

FIG. 3. $C_{l\alpha}$-polars of the 2D-airfoil geometry of the *T-FLEX* wingtip at different Reynolds numbers. [1]

The black solid graphs represent the Reynolds numbers at the wing tip of the *T-FLEX* demonstrator at the expected stall speed. An increasing deviation in Reynolds number shows an increasing change in the $C_{l\alpha}$ and $C_{m\alpha}$ polars. The progression for the Re = 60000 polars have an average deviation from that of the Re = 300000 polar of more then 10%, hence a scale factor resulting in these low Reynolds number regions needs to be avoided.
The conclusion of the airfoil simulations is that the *DeFStaR* needs to be built as big as possible. With the knowledge from the simulations and the constraints derived in the conceptional design phase a scale factor of *n* = 0.53 was determined, limited by the maximum machining size of wing molding forms at the Institute of Aircraft Design. Knowing the exact scale factor, the Reynolds number at the wing tips can be calculated for the stall speed derived by hand book methods. This information is used to simulate the pressure distribution around the airfoil and compare it to the pressure distribution of *T-FLEX* at its stall condition. The resulting curves of pressure coefficient C_p are shown in Fig. 5.

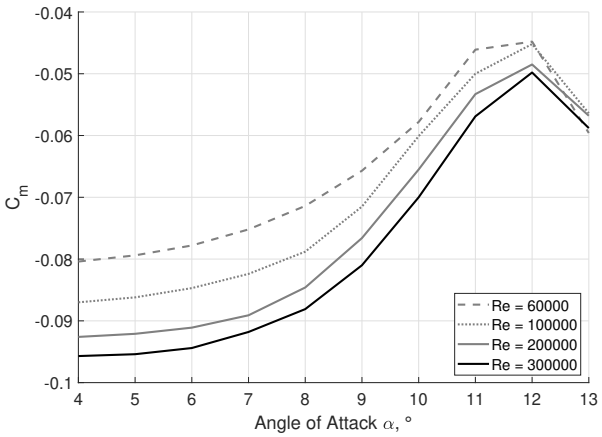

FIG. 4. $C_{m\alpha}$-polars of the 2D-airfoil geometry of the *T-FLEX* wingtip at different Reynolds numbers. [1]

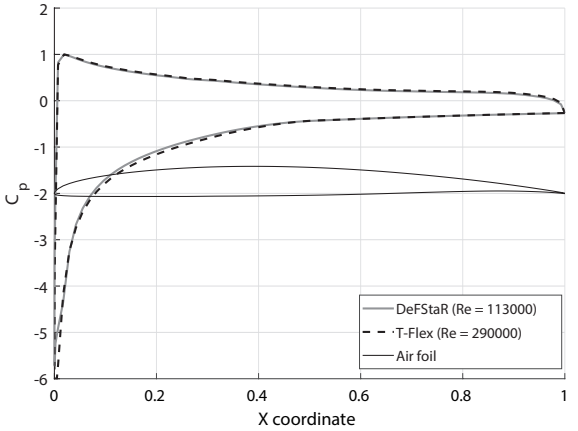

FIG. 5. C_p-polars of the 2D-airfoil geometry of the *T-FLEX* wingtip at 13° angle of attack α. [1]

The C_p-polars of *DeFStaR* and *T-FLEX* exhibit nearly identical shape, indicating good similarity on airfoil level.

3.3. Aircraft Configuration Design

In order to recreate the stalling behavior of the *T-FLEX* demonstrator, the aerodynamics of the *DeFStaR* must match

the properties on configuration level as well. However, the use of COTS components can cause deviations from the exact development aim. Therefore, when relying on COTS components to decrease development and manufacturing time and costs, it is indispensable to include the resulting constraints early into the design process. That gives the advantage to either reevaluate the choice of the component or plan for necessary modifications. A COTS fuselage as it is used for *DeFStaR*, for example, already specifics wing incidence angle, stabilizer incident angle and distance between empennage and wing. Combined with a COTS empennage the tail volume coefficient V_H is already set. To achieve comparability of the recovery process after the aircraft stalled it is important that the horizontal tail volume coefficient as a measure of lateral control and stability matches between *T-FLEX* and *DeFStaR*. With this consideration and a *XFLR5* [14] analysis it was deduced that the an extension of the tail boom by 290 mm causes the least amount of manufacturing effort.
With the knowledge of the aircraft geometry derived from a down-scaled *T-FLEX* wing, a 3-D Scan of the COTS fuselage and empennage as well as the calculated mass and mass the inertia according to the scaling laws, *DeFStaR* was analysed on configuration level and compared to the results of the *T-FLEX* configuration in terms of aerodynamic derivatives $C_{L\alpha}$ and $C_{m\alpha}$. To influence the polars of the *DeFStaR* adjustments to the longitudinal location of the C.G. and the elevator trim were made. The resulting plots of the *XFLR5* [14] analysis are depicted in Fig. 6 and 7.

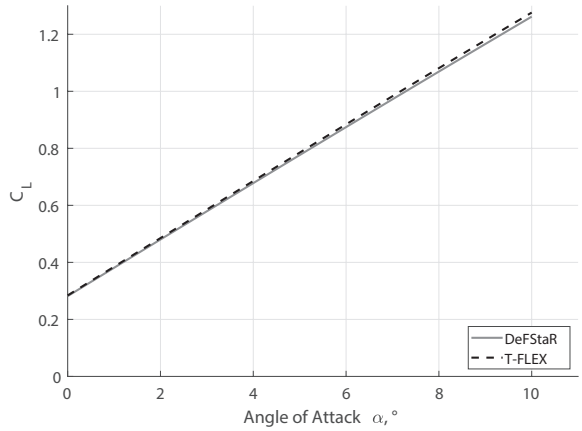

FIG. 6. $C_{L\alpha}$-polars of demonstrators *T-FLEX* and *DeFStaR*. [1]

The graphs attest a good similarity regarding the progression of the $C_{L\alpha}$ and $C_{m\alpha}$ polars, hence, the configuration was accepted.

3.4. Mechanical Design and Manufacturing

To achieve a detailed design that lives up to the expectations through the simulations the mechanical design on one hand needs to carried out very conscientiously and on the other hand leave enough leeway for adjustments concerning the

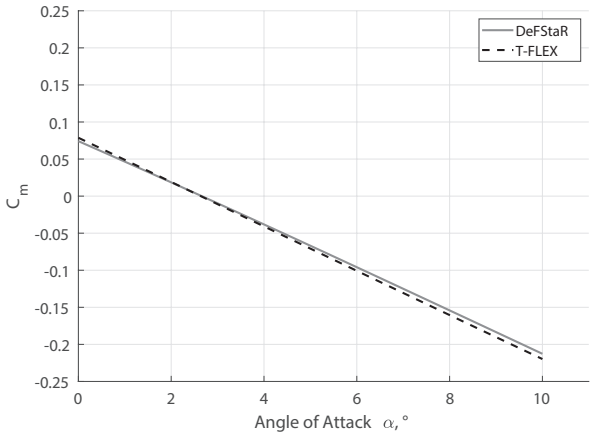

FIG. 7. $C_{m\alpha}$-polars of demonstrators *T-FLEX* and *DeFStaR*. [1]

weight an placement of the equipment that needs to be integrated. The design of the *DeFStaR* demonstrator was implemented in the CAD system *Dassault CATIA V5R19*, the resulting CAD-model is shown in Fig. 8.

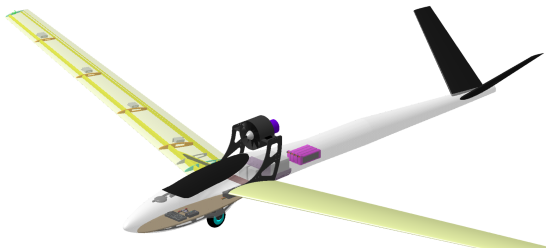

FIG. 8. Detailed model of the *DeFStaR* demonstrator implemented in *Dassault CATIA V5* [1].

The CAD-model's level of detail allowed the manufacturing of components using a 3D-printer and 3-axis CNC-router. As soon as Commercial-Off-the-Shelf (COTS) components were available, they were digitized (by measuring the major dimensions or e.g. in case of the fuselage using 3D-scanning), weighed and placed in the CAD-model. This allowed the monitoring of the C.G. and mass moments of inertia of the design. The molds for the wing as well as the carbon fiber composite wings themselves were built in-house and were the largest single activity in the manufacturing process. Additional components that could not be acquired from a supplier include: engine mount, equipment bay, undercarriage, battery bay and the tail boom extension for which the fuselage was cut, separated, and the inter-space between the parts merged with layers of carbon fiber composite deposited in a 3-D printed molding form.

4. DEMONSTRATOR TESTING

4.1. Derivation of Test Plan

The test plan followed a 3-step approach: First, tests aiming at assuring the safe operation of the demonstrator were conducted. Second, assessment of the degree of dynamic as well as aerodynamic similitude in ground and flight tests as well as finally the actual stall tests. A more detailed list is given below:

1. Assuring air-worthiness:
    - Testing of components and systems, including actuators, propulsion system and power supply a.o.
    - Free-field range tests.
    - Static load tests.
    - Maiden flight with increased static margin, in flight system tests.
    - Envelope expansion with projected static margin.
2. Assuring dynamic as well as aerodynamic similitude:
    - Weight and balance tests.
    - Bifilar pendulum tests to derive the mass moments of inertia.
    - Identification of aerodynamic coefficients $C_{L\alpha}$ and $C_{m\alpha}$ using multisine excitation signals during flight tests.
3. Actual stall tests.

In the following sections, the implementation of aforementioned tests is described in greater detail.

4.2. Airworthiness

The described airworthiness tests are qualitative pass/no-pass tests based on experience that proved to be adequate for the given aircraft size. Evaluation was conducted based on observation and were not planned to require additional instrumentation.
Systems test were conducted to ensure desired behavior of actuators, controllers and instrumentation equipment. Special emphasis was put on testing the behavior of safety critical aspects like loss of control link and the range test to assure sufficient signal quality with the chosen receiver location.
In order to test the structural strength of the custom built wings, a load test was conducted using four weights to approximate the wing loading due to the aerodynamic lift in terms of shear force Q_a as well as bending moment M_a along the wingspan b. The aerodynamic load distribution was determined for horizontal flight using the program *AVL 3.37* and scaled up to a 3 g-loadcase, assuming that the relative, local increase of lift force is proportional in every section. The resulting load in terms of shear force Q_w and bending moment M_w is shown in the following Fig. 9.

4.3. Dynamic and Aerodynamic Similitude

In order to assure the dynamic similitude of the demonstrator, bifilar pendulum tests were conducted to assess the mass moments of inertia of the implemented demonstrator and serve as a base for later adjustment and tuning. In order to investigate the aerodynamic similitude of aerodynamic derivatives $C_{L\alpha}$ and $C_{m\alpha}$, flight tests were planned.

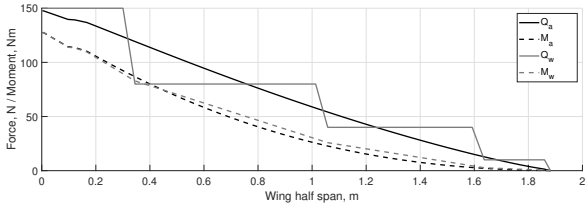

FIG. 9. Plot of the expected aerodynamic shear force Q_a and aerodynamic bending moment M_a (black) and the approximation using discrete weights of shear force Q_w and bending moment M_w (grey) [1].

4.3.1. Dynamic Similitude

In laboratory conditions, the weight and balance of the demonstrator was determined using a system consisting of two scales used for RC-aircraft. On the flight field, a single scale was used and the location of the C.G. determined by balancing the demonstrator on an edge.
The mass moments of inertia were determined using the bifilar pendulum method due its simplicity, minimal required equipment and extensive description in literature (see a.o. Jardin and Mueller [16, 17]).
In an experiment, the UAV is hung by two strings in horizontal orientation, thus creating a torsional pendulum. After initial deflection and release of the pendulum, the rotational oscillation is recorded using a camera from above. A time series of the deflection angle Θ of the bifilar pendulum is subsequently determined from the video recording using the video analysis software *Tracker 6* [18]. For determining the observed oscillation angular rate ω from the time series, a range of methods such as curve-fitting, parameter estimation or Fast Fourier-Transformation (FFT) are available.

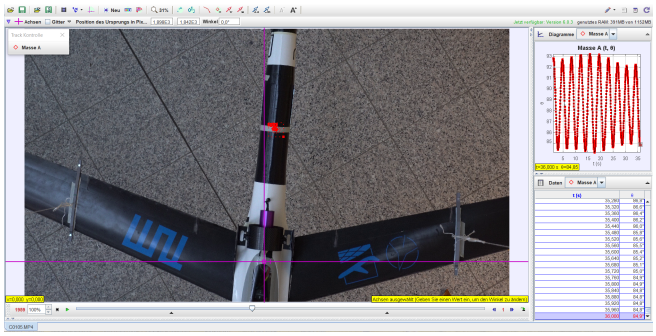

FIG. 10. Exemplary creation of a time series of deflection angle Θ from a video recording using the video analysis software *Tracker 6* [18, 1].

Finally, the mass moment of inertia can be calculated with equ. 1 using the demonstrator mass m, the gravitational constant g, the distance between the two strings D and the height

of the pendulum h (i.e. the lengths of the strings).

$$I = \frac{mgD^2}{4h\omega^2} \tag{1}$$

The described approach accepts a range of simplifications by neglecting the influence of air accelerated by the moving surfaces, the mass of strings and assumes the strings of identical length and parallel orientation. Further more, it needs to be noted that the mass moments of inertia are determined in the body-fixed frame, while the flight test experiments will be evaluated in the stability-axis frame.

4.3.2. Aerodynamic Similitude

As the design focused on achieving similarity of aerodynamic derivatives $C_{L\alpha}$ and $C_{m\alpha}$ as the driving values to represent the stall behaviour, flight tests aiming at the identification of a state space model of the short-period mode and calculate the values of the aerodynamic derivatives $C_{L\alpha}$ and $C_{m\alpha}$ from the respective parameters. A reduced state space model of the short-period mode is given in equ. 2 with a simple formulation of the output equation (equ. 3), neglecting cross-coupling of other eigen-modes [19].

$$\begin{bmatrix} \dot{\alpha} \\ \dot{q} \end{bmatrix} = \begin{bmatrix} Z_\alpha & Z_q + 1 \\ M_\alpha & M_q \end{bmatrix} \cdot \begin{bmatrix} \alpha \\ q \end{bmatrix} + \begin{bmatrix} Z_\eta \\ M_\eta \end{bmatrix} \cdot \begin{bmatrix} \eta \end{bmatrix} \tag{2}$$

$$\begin{bmatrix} \alpha \\ q \end{bmatrix} = \begin{bmatrix} 1 & 0 \\ 0 & 1 \end{bmatrix} \cdot \begin{bmatrix} \alpha \\ q \end{bmatrix} + \begin{bmatrix} 0 \\ 0 \end{bmatrix} \cdot \begin{bmatrix} \eta \end{bmatrix} \tag{3}$$

Previous tests yielded difficulties identifying the state space parameter Z_η, representing the lift due to elevator deflection η, and the state space parameter Z_q, representing lift due to pitch-rate q, most likely due to the small contribution to overall lift [20]. Aforementioned state space parameters are therefore set to 0, simplifying the state space model further to the form presented in equ. 4:

$$\begin{bmatrix} \dot{\alpha} \\ \dot{q} \end{bmatrix} = \begin{bmatrix} Z_\alpha & 1 \\ M_\alpha & M_q \end{bmatrix} \cdot \begin{bmatrix} \alpha \\ q \end{bmatrix} + \begin{bmatrix} 0 \\ M_\eta \end{bmatrix} \cdot \begin{bmatrix} \eta \end{bmatrix} \tag{4}$$

After identification of the state space parameters presented in equ. 4, the aerodynamic coefficients can be determined using the relations given in equ. 5ff:

$$[C_{L\alpha} + C_D|_0] = -\frac{Z_\alpha m v_0}{\bar{q} S} \tag{5}$$

$$C_{m\alpha} = \frac{M_\alpha I_{yy}}{\bar{q} S \bar{c}} \tag{6}$$

$$C_{mq} = \frac{2 v_0 M_q I_{yy}}{\bar{q} S \bar{c}^2} \tag{7}$$

$$C_{m\eta} = \frac{M_\eta I_{yy}}{\bar{q} S \bar{c}} \tag{8}$$

in combination with the aircraft mass m, trimmed airspeed v_0, dynamic pressure $\bar{q}$ and reference wing area S.
In order to identify the state space parameters Z_α, M_α, M_q and M_η of the equ. 5, the following values need to be recorded during the flight test: The states angle of attack α and pitchrate q together with their derivatives $\dot{\alpha}$ and $\dot{q}$ as well as input in from of the elevator deflection η. To acquire the data, a *Pixhawk 4* board was installed, which runs *PX4* autopilot software for recording a custom selection of messages, containing a range of values. A selection of the recorded values together with the available logging rates is given in Table 2.

TAB. 2. Messages with values and logging rates recorded by the PX4-autopilot used as a data acquisition system.

Value		**Logging Rate** [Hz]
Differential pressure	p_d	100
Temperature	T	100
RC inputs		45
Barometric Altitude	h_b	20
Barometric Pressure	p_b	20
Angular Velocities	p, q, r	280
Attitude (quaternions)		200
Global Position		2
Local Position		100

Please note that not all values are measured directly, but are either estimated and logged during flight (attitude values) or calculated from estimated values during data analysis such as the angle of attack α which is estimated from the aerodynamic velocities estimated in the NED-frame after transformation into the body-fixed frame.
Flight experiments were planned similarly to the description of Sobron et al. [21] and Morelli [22, 23], by superimposing multi-sine elevator signals on the pilots stick inputs. The practical implementation utilized an *Arduino nano*-board [24] serving as a multiplexer between the RC-receiver and the actuators moving the V-tail. The multiplexer reads a total of four channels: one channel for each of the actuators in the left and right control surface, one channel enabling the pilot to switch the superposition of the multi-sine signal active/inactive, the fourth channel is read from an additional RC-receiver communicating with a second transmitter and serves the adjustment of amplitude A of the superimposed signal. In case of deactivated superposition, the signals from the RC-receiver to the actuators are read and forwarded directly to the actuators in the V-tail, when the superposition of the multi-sine signal is activated by the pilot, the momentary values of the multi-sine are calculated onboard the multiplexer and added to the signals read from the RC-receiver before forwarding the signals to the actuators. During a flight test, the pilot trims the aircraft for straight and level flight and activates the signal superposition. In the first test point, the amplitude A of the signal is set to 0 and is only slowly increased by a second person using the secondary transmitter. When the amplitude A is deemed appropriate, further test points are conducted at the same trimmed airspeed v_0 and amplitude A. This procedure allows for an cautious, exploratory implementation of flight tests, in which the pilot can concentrate on the safe operation of the aircraft.

4.4. Stall Tests

The stall behavior was planned to be assessed during flight tests by initiating a stall by reducing airspeed v while trying to maintain altitude. Tufts were attached to the wing and filmed by a video camera to assess the progression of flow separation over the wing. Two different flap settings were tested, one flap setting representative for a take-off configuration as well as a landing configuration resembling the respective flap configuration as applied to the *T-FLEX* demonstrator. The flap settings were chosen, because a stall was deemed most likely during these two flight phases. Flap angles were determined using the tool *GliderThrow* angle meter featuring a resolution of 0.1 ° [25].

5. TEST RESULTS

Tests concerning the airworthiness described in chapter 4.2 were assessed qualitatively and sufficed the set heuristic criteria. Maiden and envelope expansion flights followed the heuristic procedure of flying with increased static margin ("nose-heavy"), followed by flights with gradually reduced static margin until the projected value was reached, and envelope expansion as the trust in the system increased. In the following the evaluation and results of tests concerning the demonstrators intended similitude (chapter 4.3) and stall characteristics (chapter 4.4) is described in more detail.

5.1. Bifilar Pendulum Tests

Several experiments around each axis were conducted before the first flight. Two experiments for each of the body-fixed axes were analysed by creating a time series of the deflection angle Θ using the the video material of the tests and the video analysis software *Tracker 6*. The oscillation angular rate ω was determined by applying a FFT to the data, which yielded a very prominent peak like given in the following Fig. 11 as an example.

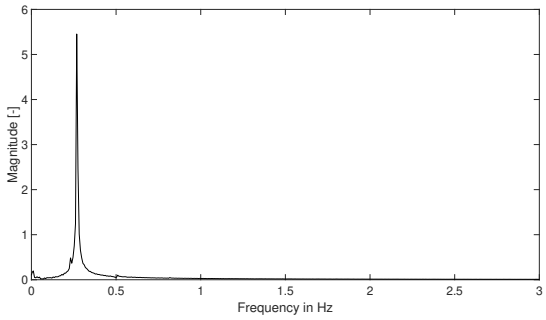

FIG. 11. Exemplary Fast-Fourier-Transform of the bifilar pendulum oscillation featuring a prominent peak indicating the observed angular rate ω [1].

The mass moments of inertia were calculated according to equ. 1, results of the experiments are presented in Table 3 together with the intended values of each mass moment of inertia.

TAB. 3. Results of the bifilar pendulum tests to determine the mass moments of inertia [1]. .

	$I_{xx}\ [kgm^2]$	$I_{yy}\ [kgm^2]$	$I_{zz}\ [kgm^2]$
Test 1	2,77	1,20	3,40
Test 2	2,41	1,22	3,55
Average	2,59	1,21	3,46
Target	2,81	1,13	3,92
Deviation	-7,82%	7,1%	-13,2%

As becomes apparent, the results for the mass moment of inertia I_{yy}, required to calculate the aerodynamic derivatives $C_{L\alpha}$ and $C_{m\alpha}$ in equ. 5f, deviate. The average value is about 7% larger than the intended value. While an increase in mass moment of inertia is easily implemented by adding masses, a decrease necessitates a grouping of components closer to the center of gravity (C.G.), which was unfeasible in this case due to the already tight component layout in the fuselage. Therefore, it was decided to keep the increased mass moment of inertia I_{yy} in mind and redesign if deemed necessary after the flight tests for identifying the short-period mode.

5.2. System Identification Flight Tests

System identification flights were conducted with two different configurations: The configuration with increased static margin as part of the system tests with the goal to assess the methodology consisting of signal amplitude selection and injection, data logging, post-processing, and analysis using MATLAB's System Identification toolbox with the *greyest*-function. The projected function resembling the configuration simulated in *XFLR5* (see Fig. 6 and 7) was planned to be tested on a second test day.
For data evaluation the time periods, in which multi-sines were superimposed, were analysed. The time periods, which the superposition was switched on could easily be identified by plotting the RC-channel used to switch the state of the multiplexer board (see section 4.3). Post-processing included the adding of the superimposed signal using the noted amplitude value and known signal shape as well as conversion to elevator deflection using an approximated function based on PWM-signal to flap deflection mapping. The angle of attack α was calculated from the aerodynamic velocities in the body-fixed frame derived from the values in the *Local Position*-messages (see Table 2). After assembling the inputs and outputs, the parameters of the state-space model given in equ. 4 were estimated using the function *greyest*. The assessment of the results is done according the maximal cross-correlations ρ_{max} in the data-set: According to Jategaonkar [26], results are acceptable if the maximum cross-correlation ρ_{max} between the state-space parameters display maximum values of $\rho_{max} = 0.9$. This criterion was applied for the selection of data points.
On the first test day, 15 maneuvers were conducted, of which five yielded a maximum cross-correlations $\rho_{max} \leq 0.9$ and were accepted for comparison with simulation results. On the

second test day, seven out of nine test points were accepted. The results are compiled in the following Tables 4 and 5

TAB. 4. Identified state-space parameters and calculated aerodynamic derivatives resulting from the flight tests conducted on the first test day. [1]

Set	ρ_{max}	Z_α	$C_{L\alpha} + C_D\|_0$	M_α	$C_{m\alpha}$
1.1	0.88	-8.23	5.68	-100.61	-1.57
1.2	0.77	-6.65	5.22	-75.39	-1.52
1.3	0.79	-5.74	4.35	-106.05	-1.98
1.4	0.9	-7.22	5.36	-86.42	-1.55
1.5	0.81	-6.33	5.32	-84.12	-1.91
Average			**5.19**		**-1,71**
95%-Confidence Bounds			**±0.62**		**±0.27**

TAB. 5. Identified state-space parameters and calculated aerodynamic derivatives resulting from the flight tests conducted on the second test day. [1]

Set	ρ_{max}	Z_α	$C_{L\alpha} + C_D\|_0$	M_α	$C_{m\alpha}$
2.1	0.81	-8.43	6.46	-88.25	-1.72
2.2	0.89	-6.68	5.94	-59.75	-1.56
2.3	0.71	-5.01	4.64	-40.32	-1.14
2.4	0.89	-7.09	6.40	-49.78	-1.34
2.5	0.82	-5.52	4.87	-44.35	-1.14
2.6	0.89	-6.59	6.17	-57.84	-1.67
2.7	0.84	-5.16	4.78	-47.76	-1.34
Average			**5.61**		**-1.42**
95%-Confidence Bounds			**±0.75**		**±0.22**

5.3. Stall Tests

Stall tests were flown with the configuration of the second test day. For inducing a stall, the engine was switched off while the elevator deflection was steadily increased to maintain altitude while the demonstrator decelerated. A total of 15 stall tests were conducted in flap configurations representing the take-off and landing configurations of the *T-FLEX* demonstrator. The deflections for the four flaps on each wing are stated in the Table 6:

TAB. 6. Flap configurations tested.

Configuration	Take-off (TO)	Landing (LD)
Flap 1	8.3°	23.3°
Flap 2	6.2°	0°
Flap 3	4.4°	0°
Flap 4	1.2°	0°

The stall events were evaluated qualitatively, based on the video footage of the onboard camera filming the left wing equipped with tufts as well as the camera on ground tracking the aircraft. An overlay of both materials is provided for a selection of test points under the link below and gives an impression about the different observed stall behavior:

https://youtu.be/ZE44NFiudh8

As becomes apparent from the overlay provided, the demonstrator displayed different stall onset locations and a variety of stalling behaviors, including rolling to the left and right as well as a flat spin and a "plunging" flight state, which is characterized as a flight state, in which the demonstrator rapidly looses altitude, but is able to maintain attitude and retain rolling control authority. The selection of stall tests presented in the video are listed in the Table 7 below:

TAB. 7. Overview of the stall tests conducted, location of stall-onset and observed behavior as presented in the video overlay.

No.	Flaps	Stall onset	Behavior
3	LD	Wing tip	-
4	LD	Wing root	Plunging flight.
5	LD	Wing tip	Rotation to the left.
6	LD	Wing tip	Plunging flight.
7	TO	Wing root	Rotation to the right.
8	TO	Wing tip	Rotation to the left. Flat spin.

With the two flap configurations selected, no clear trend emerged in terms of location of stall onset or stalling behavior during the number of flight tests conducted.

6. DISCUSSION, OUTLOOK AND LESSONS LEARNED

The publication describes the design process, implementation as well as ground and flight testing of the *DeFStaR* demonstrator, built for the purpose of assessing the stall behavior of the *T-FLEX* demonstrator. The scaling focused on the geometrical scaling of the wing and configurations as well as dynamic scaling in terms of mass distribution, i.e. mass moments of inertia. Besides the tests assuring airworthiness, both ground and flight tests for assessing the weight and balance, the mass moments of inertia as well as the aerodynamic derivatives $C_{L\alpha}$ and $C_{m\alpha}$ were conducted before the demonstrator's stall behavior was assessed.
In terms of geometric similitude of the wing, close resemblence can be expected due to the chosen manufacturing process of hand-lay-up into a negative, polished mold. Also the flow condition over the 2D-airfoil is expected to be similar due to a forced transition at 5% chord-length present on both aircraft, even though the Reynolds numbers differ. In terms of resulting aerodynamic coefficients C_l and C_m of the 2D-airfoil, different absolute values are predicted, the trend with increasing angle of attack α, however, is represented well over the range of relevant Reynolds numbers. On configuration level, the *DeFStaR* demonstrator displays similar values in terms of aerodynamic derivatives $C_{L\alpha}$ and $C_{m\alpha}$, which compared rather well with the short-period identification flight test results. In Fig. 12 and 13, the aerodynamic coefficients C_L and C_m are plotted over the angle of attack α. Please note two assumptions: Firstly, the polars of the *DeFStaR* demonstrator are plotted with an intersection at an angle of attack $\alpha = 0°$, i.e. assuming same values for the aerodynamic coefficients C_{L0} and C_{m0}, since the instrumentation only allowed the identification of the aerodynamic deriva-

tives $C_{L\alpha}$ and $C_{m\alpha}$ (Fig. 12 and 13). Secondly, the identified values incorporate the contribution of the drag coefficient in the trimpoint $C_{D|0}$ (compare to equ. 5), which is considered negligible small in comparison to the contribution from the aerodynamic derivative $C_{L\alpha}$ (Fig. 12).

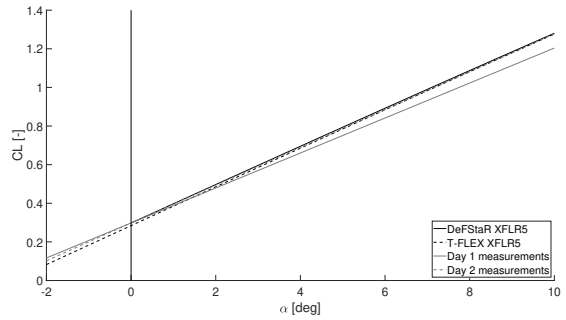

FIG. 12. Comparison of the identified values to the simulated values of the aerodynamic derivatives $C_{L\alpha}$ [1].

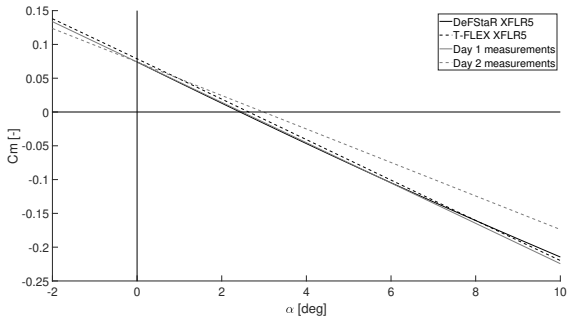

FIG. 13. Comparison of the identified values to the simulated values of the aerodynamic derivatives $C_{L\alpha}$ [1].

In Fig. 12, the aerodynamic derivatives $C_{L\alpha}$ compare well with only the value of the day 1 flight testes yielding a smaller value than projected. This, however, matches the expectation due to the larger static margin ("nose-heavy" configuration). On the other side, due to the rather large scatter of the flight test results, it cannot be excluded that the actual value was identical to the projected value.

A similar picture is displayed in Fig. 13: Here the identified value for the aerodynamic derivative $C_{m\alpha}$ matched well with the exemption of the result of day 2 flight test regards. Even when considering the 95%-confidence interval the projected value is not being reached. An investigation of this issue found a COG that was placed too far aft, reducing the static margin and thus explaining the value for the aerodynamic derivative $C_{m\alpha}$. In terms of stall tests, the configuration flown on day 2 can be expected to have a projected stall speed. The reduced value of the aerodynamic derivative $C_{m\alpha}$, however, might change the stall behavior, even though it is assumed, that the qualitative behavior does not change.

Therefore, it is concluded that the aerodynamic scaling resembles the design of the *T-FLEX* demonstrator sufficiently well, at least in a range of angle of attack α, in which the aerodynamic derivative $C_{L\alpha}$ remains constant. If the aerodynamic similitude retains in the regime in which stall occurs cannot be known with certainty with the presented approach, however, the similar, simulated pressure distributions give an indication that sufficient similarity can be assumed.

In terms of dynamic similitude, the bifilar pendulum tests revealed deviations of up to 13.2%. The mass moment of inertia I_{yy}, was found to be 7.1% larger than projected. These deviation are assumed to be larger than the errors introduced by the method of testing and the fact, that the mass moments of inertia were determined in the body-fixed frame and not transformed into the stability frame before calculating the aerodynamic derivatives (equ. 5f). This rather large deviation, however, was finally accepted, because the projected values were based on an estimates from a CAD-model, not measurements, for the *T-FLEX* demonstrator. As comparison, by means of constant CAD-model updating during demonstrator manufacture, Jordan et al. claim to have reached a deviation of 0.1% in terms of mass for the *T-2* demonstrator and its CAD-model, which resulted in 3% deviation in mass moments of inertia [8]. Since the deviation in terms of mass between the demonstrator and its CAD-model were found to be larger for the *T-FLEX* demonstrator, larger deviations are expected for the mass moments of inertia as well.

Concerning the stall behavior, no clear trend emerged that would link the flap setting to the stall onset locations or stall behavior during the number of tests conducted. This indicates, that the resulting stall behavior is heavily dependent on the initial conditions at stall onset that have not been recorded in the study at hand. E.g. small changes in angle of sideslip might cause the demonstrator to roll to the left or right. Noteworthy is the rather unexpected range of behaviors exhibited: While in the majority of cases the demonstrator rolled to the left or right and recovered after loosing a relatively small amount of altitude, on one occasion the demonstrator entered a flat-spin in which it lost 170 m of altitude despite its short duration. On the other hand, the demonstrator twice entered a rather benign "plunging" flight state in which altitude was decreased in a rather steep glide slope, while sufficient control authority was retained to maintain attitude.

Due to the range of stall behaviors found, the project goal to assess the stall behavior of the *T-FLEX* demonstrator cannot be regarded as conclusive reached. The findings do, however, indicate possibilities for further research: Since a "plunging" flight state is to be preferred as a stall behavior for operational reasons, future work should aim at finding means to enter this flight state reliably. A possible way would be the investigation of further flaps settings in combination with the widely used simulation program *AVL* [27], which manual mentions a way to predict stall on swept, high aspect ratio wing. This investigation could further benefit from more elaborate use of tufts together with video analysis to visualize the flow over the wing and empennage, as described by Hoff & Gratton [28]. Already a reliable, qualitative prediction method for the stall behavior would be a valuable tool for aircraft designers in the future.

The characterization of the *DeFStaR* demonstrator itself could be improved by comparing the existing flight test data with more simulations, starting with simulations of the configura-

tions of day 1 and day 2, as well as the influence of the flap deflections. Especially an investigation of day 2 configuration's close match in terms of aerodynamic derivative $C_{L\alpha}$ but mismatch of aerodynamic derivative $C_{m\alpha}$ would be interesting. Further flight tests focusing on system identification and further instrumentation to record the flight state can decrease the range covered by the confidence intervals of the identified values. An air data probe recording the aerodynamic angles could greatly increase the accuracy of system identification results as well as information available from stall experiments. Determining the aerodynamic coefficients C_{m0} and C_{L0} would give further insight about the absolute deviations of the related polars of the demonstrators *DeFStaR* and *T-FLEX*. Finally, a comparison of the presented flight test results of the *DeFStaR* demonstrator with flight test results of *T-FLEX* demonstrator to assess the degree of similitude would be interesting, once comparable results are available.

Among the lessons learned is the necessity of rigorous project management and constant progress monitoring to ensure the execution as well as analysis of the relevant flight test experiments, which are typically planned to the end of the project timeline and are the first ones jeopardized by delays. In this regard a comparably small delay of two weeks in a project of twelve months can defeat its purpose because the ultimately relevant tests cannot be conducted and assessed any more. In this context it is valuable to realize, that the challenges of the project at hand lay primarily in the domain of rather trivial engineering tasks such as ensuring availability of people, machines and materials, while tasks, which are typically considered more sophisticated like flight tests/analysis for system identification, did not prolong the project timeline.

7. ACKNOWLEDGEMENTS

The work presented has been conducted within the framework of project FLiPASED (grant agreement No. 815058) funded from the European Union's Horizon 2020 research and innovation program.

The authors would like to thank Peter Geldner and Fabian Wiedemann for the technical support and piloting the *DeFStaR* demonstrator as well as Marius Weber for the support in questions related to system identification.

8. REFERENCES

[1] Bastian Scheufele. *Development, Flight-Testing and Evaluation of a Subscale Dynamic Demonstrator to Reproduce the Stall Behavior of a Large Swept Wing Research UAV*. Master thesis, Technical University of Munich, Munich, 22.11.2021.

[2] Philipp Stahl, Franz-Michael Sendner, Andreas Hermanutz, Christian Rößler, and Mirko Hornung. Mission and Aircraft Design of FLEXOP Unmanned Flying Demonstrator to Test Flutter Suppression within Visual Line of Sight. In *17th AIAA Aviation Technology, Integration, and Operations Conference 2017*, page 11, Red Hook, NY, 2017. Curran Associates Inc. ISBN 978-1-62410-508-1. doi: 10.2514/6.2017-3766.

[3] Franz-Michael Sendner. *Evaluierung und Auswahl von geeigneten Antriebslösungen für ein unbemanntes Forschungsfluggerät.* Master's Thesis, Technical University of Munich, Munich, 2016.

[4] FLEXOP, 2020. URL `https://flexop.eu/`.

[5] Alejandro Sobron, David Lundström, and Petter Krus. A review of current research in subscale flight testing and analysis of its main practical challenges. *Aerospace*, 8 (3):74, 2021.

[6] Bahman Zohuri. *Dimensional Analysis and Self-Similarity Methods for Engineers and Scientists*. Springer eBook Collection Energy. Springer International Publishing, Cham, 2015. ISBN 9783319134765. doi: 10.1007/978-3-319-13476-5. URL `http://swbplus.bsz-bw.de/bsz430171137cov.htm`.

[7] Joseph R. Chambers. *Modeling flight: The role of dynamically scaled free-flight models in support of NASA's aerospace programs*, volume 575 (2009) of *NASA SP*. National Aeronautics and Space Administration, Washington D.C., 2009. ISBN 978-0-16-084633-5.

[8] Thomas Jordan, John Foster, Roger Bailey, and Christine Belcastro. Airstar: A uav platform for flight dynamics and control system testing. In *25th AIAA Aerodynamic Measurement Technology and Ground Testing Conference*, Reston, Virigina, 2006. American Institute of Aeronautics and Astronautics. ISBN 978-1-62410-029-1. doi: 10.2514/6.2006-3307.

[9] Alejandro Sobron. *On Subscale Flight Testing: Applications in Aircraft Conceptual Design*, volume 1819. Linköping University Electronic Press, Linköping, 2018. doi: 10.3384/lic.diva-152488.

[10] Christopher Jouannet, David Lundstrom, Kristian Amadori, and Patrick Berry. Design of a very light jet and a dynamically scaled demonstrator. In *46th AIAA Aerospace Sciences Meeting and Exhibit*, page 60, Reston, Virigina, 2008. American Institute of Aeronautics and Astronautics. ISBN 978-1-62410-128-1. doi: 10.2514/6.2008-137.

[11] Thomas G. Grainer and Sherwood Hoffman. *Summary of transformation equations and equations of motion used in free flight and wind tunnel data reduction and analysis*. National Aeronautics and Space Administration, Washington D.C., 1972.

[12] C. H. Wolowicz, J. S. Bowman, and W. P. Gilbert. *Similitude Requirements and Scaling Relationships as Applied to Model Testing*. NASA technical paper. National Aeronautics and Space Administration, Washington D.C., 1979.

[13] Alejandro Sobrón. *On subscale flight testing : Cost-effective techniques for research and development*, volume 2127. Linköping University Electronic Press, Linköping, 2021. ISBN 9789179296919. doi: 10.3384/diss.diva-175520.

[14] XFLR5, 2021. URL `http://www.xflr5.tech/xflr5.htm`.

[15] XFOIL, 2013. URL `https://web.mit.edu/drela/Public/web/xfoil/`.

[16] Matthew Jardin and Eric Mueller. Optimized measurements of uav mass moment of inertia with a bifilar pendulum. In *AIAA Guidance, Navigation and Control Conference and Exhibit*, page 6822, 2007.

[17] Matt R. Jardin and Eric R. Mueller. Optimized measurements of unmanned-air-vehicle mass moment of inertia with a bifilar pendulum. *Journal of Aircraft*, 46(3):763–775, 2009. ISSN 0021-8669. doi: 10.2514/1.34015.

[18] Douglas Brown, Wolfgang Christian, and Robert M Hanson. Tracker: Video analysis and modeling tool, 2021. URL https://physlets.org/tracker/.

[19] Rudolf Brockhaus, Wolfgang Alles, and Robert Luckner. *Flugregelung*. Springer Berlin Heidelberg, Berlin, Heidelberg, 3. aufl. 2011 edition, 2011. ISBN 9783642014437. URL http://nbn-resolving.org/urn:nbn:de:bsz:31-epflicht-1564615.

[20] Adrian Emanuel Albert. *Multi-Fidelity Comparison of Flight Dynamics Models for a Turbine-driven UAV Demonstrator*. Master thesis, Technical University of Munich, Munich, 2020.

[21] Alejandro Sobron, David Lundström, Roger Larsson, Petter Krus, and Christopher Jouannet. Methods for efficient flight testing and modelling of remotely piloted aircraft within visual line-of-sight. In *ICAS 2018*. The International Council of the Aeronautical Sciences c/o Deutsche Gesellschaft für Luft- und Raumfahrt, Bonn, 2018. ISBN 978-3-932182-88-4. URL http://www.diva-portal.org/smash/record.jsf?pid=diva2%3A1295432&dswid=-149.

[22] Eugene A. Morelli. Flight test maneuvers for efficient aerodynamic modeling. *Journal of Aircraft*, 49(6):1857–1867, 2012. ISSN 0021-8669. doi: 10.2514/1.C031699.

[23] Eugene A. Morelli. Practical aspects of multiple-input design for aircraft system identification flight tests. In *AIAA AVIATION 2021 FORUM*, Reston, Virginia, 08022021. American Institute of Aeronautics and Astronautics. ISBN 978-1-62410-610-1. doi: 10.2514/6.2021-2795.

[24] Arduino Official Store. Arduino nano, 13.09.2022. URL https://store.arduino.cc/products/arduino-nano.

[25] GliderCG. Gliderthrow | glidercg, 10.05.2022. URL https://www.glidercg.com/gliderthrow.

[26] Ravindra Jategaonkar. *Flight vehicle system identification: A time domain methodology*, volume 216 of *Progress in astronautics and aeronautics*. American Institute of Aeronautics and Astronautics, Reston, Va., 2006. ISBN 9781563478369.

[27] AVL, 2017. URL http://web.mit.edu/drela/Public/web/avl/.

[28] RI Hoff and GB Gratton. Camera tracking and qualitative airflow assessment of a two-turn erect spin. *The Aeronautical Journal*, 116(1179):541–562, 2012.